

# The 3-point function in large scale structure: redshift distortions and galaxy bias

E. Gaztañaga<sup>1</sup> & R. Scoccimarro<sup>3,4</sup>

<sup>1</sup>*Instituto de Ciencias del Espacio (IEEC/CSIC), Facultat de Ciències UAB, Torre C5- Par- 2a, Bellaterra (08193 BARCELONA)*

<sup>3</sup>*Center for Cosmology and Particle Physics, Department of Physics, New York University, NY, USA*

<sup>4</sup>*Kawli Institute for Cosmological Physics, University of Chicago, Chicago, IL 60637, USA*

10 November 2018

## ABSTRACT

We study the behavior of the three-point correlation function  $\zeta$  of dark matter and mock galaxies, concentrating on the effects of redshift-space distortions and the determination of galaxy bias parameters in current redshift galaxy surveys. On large scales, redshift space distortions tend to wash out slightly the configuration dependence of the reduced 3-point function  $Q_3 \sim \zeta/\xi^2$ . On smaller scales ( $\leq 10h^{-1}\text{Mpc}$ ),  $Q_3$  develops a characteristic U-shape anisotropy between elongated and open triangles due to the effects of velocity dispersion. We show that this shape is quite universal, very weakly dependent on scale, initial spectral index or cosmological parameters and should be detectable in current galaxy surveys even if affected by shot-noise or galaxy bias. We present a detailed method for obtaining constraints on galaxy bias parameters from measurements of  $Q_3$  in current galaxy redshift surveys, based on the eigenmode analysis similar to the one developed for the bispectrum. We show that our method recovers the bias parameters introduced into mock galaxies by a HOD prescription and is also able to handle potential systematics in the case when a smaller number than ideal of mock catalogs is used to estimate the covariance matrix. We find that current redshift surveys (e.g. SDSS or 2dFGRS) are just about large enough to get interesting new constraints on bias.

## 1 INTRODUCTION

The galaxy three-point function provides a valuable statistical tool to investigate the nature of the relationship between galaxies and dark matter and to probe the statistical properties of primordial fluctuations through constraints on primordial non-Gaussianity (see Bernardeau et al. 2002 for a review).

Measurements of the three-point function and other higher-order statistics in galaxy catalogs have a rich history (Peebles & Groth 1975, Fry & Peebles 1978, Baumgart & Fry 1991, Gaztañaga 1992, Bouchet et al. 1993, Fry & Gaztañaga 1994). In the past decade, three-point statistics have confirmed the basic picture of gravitational instability from Gaussian initial conditions (Frieman & Gaztañaga 1994, Jing & Börner 1998, Frieman & Gaztañaga 1999, Feldman et al. 2001). The impact of such measurements on theoretical models has been important but the systematic and statistical uncertainties in the data have been non-negligible, primarily because the connection between these statistics and theoretical predictions is best done on large scales, where the physics is best understood, and the surveys previously available were not large enough.

In recent years, with the completion of large redshift surveys such as 2dFGRS (Colless et al. 2001) and SDSS (York et al. 2000) the measurement of higher-order statis-

tics promises to provide tight constraints at the few percent level (Colombi et al. 1998, Szapudi et al. 1999, Matarrese et al. 1997, Scoccimarro et al. 2004, Sefusatti & Scoccimarro 2004) that will help significantly in pinning down the cosmological parameters and issues in galaxy formation that have an impact on galaxy clustering. First measurements of three-point statistics in these redshift surveys are given in Verde et al. (2002), Jing & Börner 2004, Kayo et al. (2004) and Wang et al. (2004).

In this paper we study the three-point function with particular emphasis on redshift-space distortions and galaxy bias. There is a puzzling result regarding previous investigations of the 3-point function in redshift (configuration) space (Suto & Matsubara 1994, Matsubara & Suto 1994, Jing & Börner 1998, Jing & Börner 2004). They all find very little dependence of the 3-point function on triangle configuration at small scales (both in simulations and observations). This result is puzzling because one of the first things that brings attention to our eyes is the presence of the “fingers of god” in redshift-space distributions, produced by the radial component of galaxy peculiar velocities inside clusters. These rather long and thin structures should leave a clear imprint in the 3-point correlation function, with higher amplitudes for collapsed triangles. Why has this feature not been observed so far?

We also study the three-point function as a probe of galaxy bias in the framework of current surveys, and provide a detailed framework for computing reliable error estimates on bias parameters that include the covariance matrix due to non-linearities and survey geometry. We use a battery of N-body simulations and mock catalogs extracted from them with different biasing prescriptions. Our presentation follows closely the eigenmode analysis method developed for the bispectrum (Scoccimarro 2000).

A first paper of this series (Barriga & Gaztañaga 2002, paper I) presented a comparison of the predictions for the two and three-point correlation functions of density fluctuations,  $\xi$  and  $\zeta$ , in gravitational perturbation theory (PT) against large Cold Dark Matter (CDM) simulations. Here we extend these results into the non-linear regime and focus on the effects of redshift distortions and the extraction of galaxy bias parameters in galaxy surveys. This paper is organized as follows. In section 2 we review the basic definitions involving the three-point function. In section 3 we present the simulations and mock catalogs, whereas in section 4 we study the effects of redshift distortions from large to small scales. In section 5 we study in detail how to recover bias parameters from current galaxy catalogs.

## 2 THE THREE-POINT FUNCTION

### 2.1 Definitions

The two and three-point correlation functions are defined, respectively, as

$$\xi(r_{12}) = \langle \delta(r_1)\delta(r_2) \rangle \quad (1)$$

$$\zeta(r_{12}, r_{23}, r_{13}) = \langle \delta(r_1)\delta(r_2)\delta(r_3) \rangle \quad (2)$$

where  $\delta(r) = \rho(r)/\bar{\rho} - 1$  is the local density fluctuation about the mean  $\bar{\rho} = \langle \rho \rangle$ , and the expectation value is taken over different realizations of the model or physical process. In practice, the expectation value is over different spatial positions in our Universe, which are assumed to be a fair sample of possible realizations (see Peebles 1980). It is convenient to define a  $Q_3$  parameter as follows (Groth & Peebles 1977)

$$Q_3 = \frac{\zeta(r_{12}, r_{23}, r_{13})}{\zeta_H(r_{12}, r_{23}, r_{13})} \quad (3)$$

$$\zeta_H \equiv \xi(r_{12})\xi(r_{23}) + \xi(r_{12})\xi(r_{13}) + \xi(r_{23})\xi(r_{13}), \quad (4)$$

where we have introduced a definition for the "hierarchical" three-point function  $\zeta_H$ . The  $Q_3$  parameter was thought to be roughly constant as a function of triangle shape and scale (Peebles 1980), a result that is usually referred to as the hierarchical scaling. As we will see below, accurate measurements/predictions show that  $Q_3$  is not quite constant in any regime of clustering, although the variations of  $Q_3$  with scale are small compared to the corresponding changes in  $\xi$  or  $\zeta$ .

### 2.2 Triangle parametrizations: $\alpha$ vs. $v$

There are two parametrizations that are commonly used in the literature to describe the three parameters that define a triangle, each of which has advantages and disadvantages.

Since we are studying the monopole of the three-point function (averaged over all orientations of the triangle with respect to the observer), this depends on three variables. One obvious choice is the magnitude of the three sides of the triangle, described by  $\vec{r}_{12}$ ,  $\vec{r}_{23}$  and  $\vec{r}_{31} = \vec{r}_{12} + \vec{r}_{23}$ . This is reasonable since the three variables are on an equal footing (being three lengths) and if the measurement is done with some typical resolution due to the three-point function algorithm, it affects all of them in the same way.

The two most common parametrizations, however, involve a length scale, a dimensionless number (ratio of lengths), and some measure of triangle shape (another ratio of lengths or an angle). In this case the three variables may be affected by resolution (e.g. binning) in different ways. This can be important for example for the dependence on triangle shape, which is what concerns us here regarding the signature of fingers of God at small scales.

In perturbation theory, it has been customary to use the two sides of the triangle  $r_{12}$  and  $r_{23}$  (which are typically comparable in size) and the angle  $\alpha$  between them:

$$\cos(\alpha) = \frac{\vec{r}_{12} \cdot \vec{r}_{23}}{r_{12} r_{23}} \quad (5)$$

with  $0 < \alpha < 180$  deg. For small scales it has been popular to use  $r_{12}$  and  $r_{23}$ , but with later given by the ratio:

$$u = r_{23}/r_{12}, \quad (6)$$

and the third parameter given by:

$$v \equiv \frac{r_{31} - r_{23}}{r_{12}} \quad (7)$$

with the restriction  $r_{12} < r_{23} < r_{13}$ . The value of  $v$  is related to  $\alpha$  by:

$$v = \sqrt{u^2 - 2u \cos \alpha + 1} - u \quad (8)$$

In principle  $-1 < v < 1$ , but the restriction  $r_{12} < r_{23} < r_{13}$  only allows  $0 < v < 1$ . The minimum value of  $v = 0$  corresponds to  $\cos \alpha = 1/(2u)$ . Note how in this parametrization the small values of  $\alpha$  are only recovered for large values of  $u$ . For example, for  $u = 1$  we are restricted to  $60 < \alpha < 180$  deg. This can have implications for the detection of sharp dependencies on triangle shape, as we shall see in section 4.

Elongated or "collapsed configurations" are those with  $\alpha \simeq 0$  or  $\alpha \simeq 180$  deg; or in terms of  $v$ , those with  $v$  close to unity. Configurations of triangles with  $\alpha \simeq 90$  are called here "perpendicular" configurations. In terms of  $v$  they correspond to small values of  $v$ , but note that there is no one-to-one correspondence. Small values of  $v$  could also arise for triangles with  $r_{31} = r_{23}$  even if  $r_{12}$  is not small.

We use the term "strong configuration dependence" when there is a significant difference between the collapsed and the perpendicular configurations. By "weak configuration dependence" we mean that  $Q_3$  is hierarchical (ie constant as a function of  $\alpha$ ).

### 2.3 3-point Function Estimator and Algorithm

We follow the fast algorithm described in some detail in paper I. This algorithm allows a fast calculation of two and three-point function for millions of points. The first step is to discretize the simulation box into  $Lsize^3$  cubic cells. We assign each particle to a node of this new latticed box using

	$\Lambda$ CDM400	SCDM400	$\Lambda$ CDM	$\tau$ CDM	OCDM	SCDM	VLS	GIF	HV
$\Omega_m$	0.3	1.0	0.3	1.0	0.3	1.0	0.3	0.3	0.3
$\Omega_\Lambda$	0.7	0.0	0.7	0.0	0.0	0.0	0.7	0.7	0.7
$h$	0.7	0.5	0.7	0.7	0.7	0.5	0.7	0.7	0.7
$\Gamma$	0.2	0.5	0.2	0.2	0.2	0.5	0.16	0.21	0.16
$\sigma_8$	1.0	1.0	0.9	0.51	0.85	0.51	0.9	0.9	0.9
$N_{\text{par}}$	126 <sup>3</sup>	126 <sup>3</sup>	256 <sup>3</sup>	256 <sup>3</sup>	256 <sup>3</sup>	256 <sup>3</sup>	512 <sup>3</sup>	256 <sup>3</sup>	1000 <sup>3</sup>
$L_{\text{size}}$	400	400	240	240	240	240	479	141	3000

**Table 1.** Main parameters describing the simulations. Box size  $L_{\text{size}}$  is in  $h^{-1}$ Mpc. For VLS and HV the shape parameter  $\Gamma$  stands for an effective value corresponding to the linear power spectrum with a transfer function for  $\Omega_m = 0.26$ ,  $\Omega_b = 0.04$  and  $\Omega_\Lambda = 0.7 = h$ .

the nearest grid point particle assignment. We precalculate the list of relative neighbors to any given node in the lattice. To compute now the two-point and three-point correlation functions we use:

$$\xi(r_{12}) = \frac{\sum_{i,j} \delta_i \delta_j}{\sum_{i,j} 1} \quad (9)$$

$$\zeta(r_{12}, r_{23}, r_{13}) = \frac{\sum_{i,j,k} \delta_i \delta_j \delta_k}{\sum_{i,j,k} 1} \quad (10)$$

where  $i$  extends over all nodes in the lattice,  $j$  over the list of precalculated neighbors (see paper I) that are at a distance  $r_{12}$  from  $i$  and  $k$  over the neighbors at distance  $r_{23}$  from  $j$  and  $r_{13}$  from  $i$ .

Besides the tests presented in Barriga & Gaztañaga (2002) we have performed a series of additional tests designed to quantify how robust our new findings are in redshift space and on smaller scales. We have checked that very similar results are obtained for different pixel sizes. Pixels can be as large as  $r_{12}/3$  on a side with negligible effects in the resulting  $Q_3(\alpha)$ . This of course imposes a constraint on how thick we can take the binning in  $\alpha$  and works as long as  $Q_3$  has a smooth shape as a function of  $\alpha$ . As we will show below (ie Fig.5) the pixel scale or the binning play an important role on small scales.

Dilution of point density by factors of 1/10 or 1/20 does not bias the results, indicating that the above estimator is robust. Using realistic mock catalogues (eg. with a 2dFGRS or SDSS mask) instead of cubical boxes gives very similar results. In addition, the LCDM240 and LCDM400 simulations (see table 1 below) give values of  $Q_3$  in excellent agreement at small scales.

### 3 SIMULATIONS

We use several sets of simulations centered around the Lambda Cold Dark Matter model ( $\Lambda$ CDM from now on) with  $\Omega_\Lambda = 0.7$ ,  $\Omega_m = 0.3$ ,  $h = 0.7$ . The first set, which we call  $\Lambda$ CDM400, consist of 5 independent realizations of  $\Lambda$ CDM model normalized to  $\sigma_8 = 1$  in a box  $L = 378h^{-1}$ Mpc with  $N = 126^3$  particles. These simulations were run with the AP3M code of Efstathiou et al. (1985) to study volume-averaged higher-order correlations (see Baugh

& Gaztañaga 1996 for more details). The particle mass is  $M \simeq 2.3 \times 10^{12} M_\odot / h$ .

A second set, which we just call  $\Lambda$ CDM240 consists on a single realization of the  $\Lambda$ CDM model normalized to  $\sigma_8 = 0.9$  in a box  $L = 239.5h^{-1}$ Mpc with  $N = 256^3$  particles. This simulation was run with a parallel version of the AP3M code by the VIRGO consortium. The particle mass is  $M \simeq 6.9 \times 10^{10} M_{\text{sun}} / h$ . Thus, while a single  $\Lambda$ CDM400 has  $\simeq 4$  times more volume (20 times more volume if we use all 5 realizations) the  $\Lambda$ CDM240 model has  $\simeq 33$  times higher particle density (and therefore 33 times higher mass resolution). This will allow us to explore how  $Q_3$  is affected by resolution and sampling effects. The difference in normalization ( $\sigma_8 = 1.0$  compared to  $\sigma_8 = 0.9$ ) is quite small and has very little impact on  $Q_3$ .

We also study three further different models using simulations from the VIRGO consortium with identical volume and number of particles as  $\Lambda$ CDM240. The different models are listed in Table 1. The comparison with the SCDM allows us to study the dependence of  $Q_3$  on the shape parameter  $\Gamma$ , while the rest of the models explore sensitivity to cosmological parameters and normalization.

Finally, we consider two other simulations from the VIRGO consortium, the GIF (higher resolution), VLS (larger volume) and HV (even larger volume but with lower resolution) simulations, also shown in Table 1. These in particular were used to build the galaxy mock catalogs by using the Halo Occupation Distribution (HOD) formalism (Ma and Fry 2000, Peacock and Smith 2000, Seljak 2000, Scoccamarro et al. 2001, Berlind et al 2003, see Cooray and Sheth 2002 for a review), see Section 5.1 for details.

### 4 $Q_3$ IN REDSHIFT SPACE

Redshift distortions (Jackson 1972, Sargent and Turner 1977, Peebles 1980, Kaiser 1987) due to peculiar velocities along the line of sight create an anisotropic galaxy distribution with a preferred direction, that joining the observer to the each galaxy. Therefore different survey geometries will be affected differently by redshift distortions. Here we focus on the long-distance observer approximation where we place the observer in one of the axes at infinity. This allows a general study of redshift distortions, independent of the survey geometry. Nevertheless we do not find strong differences for

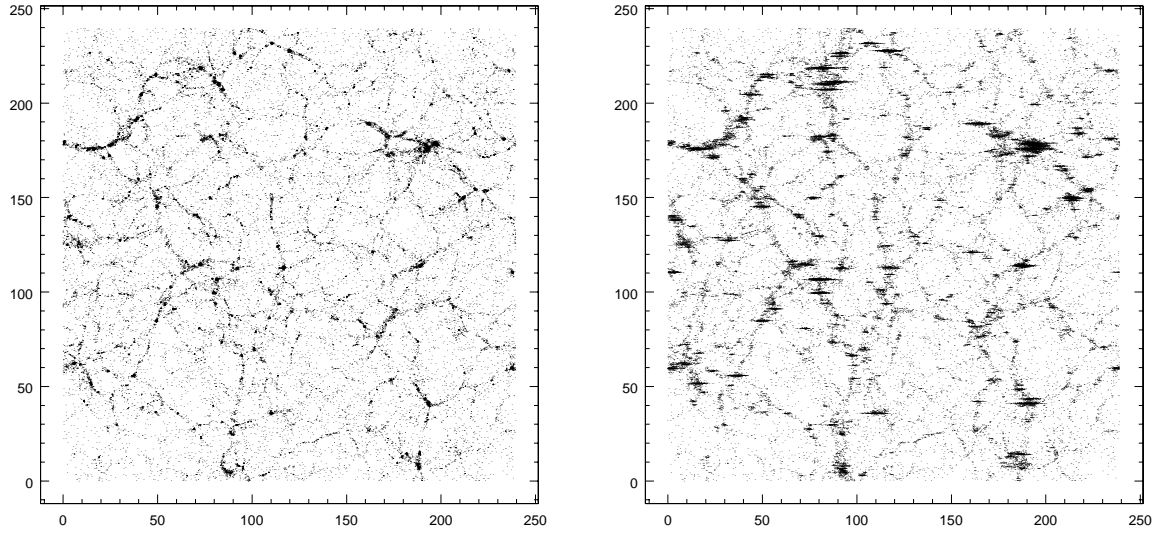


**Figure 1.** Particle positions in real (left) and redshift space (right) in a 1 Mpc/h thick projected slice from to the LCDM240 simulation (see table 1).

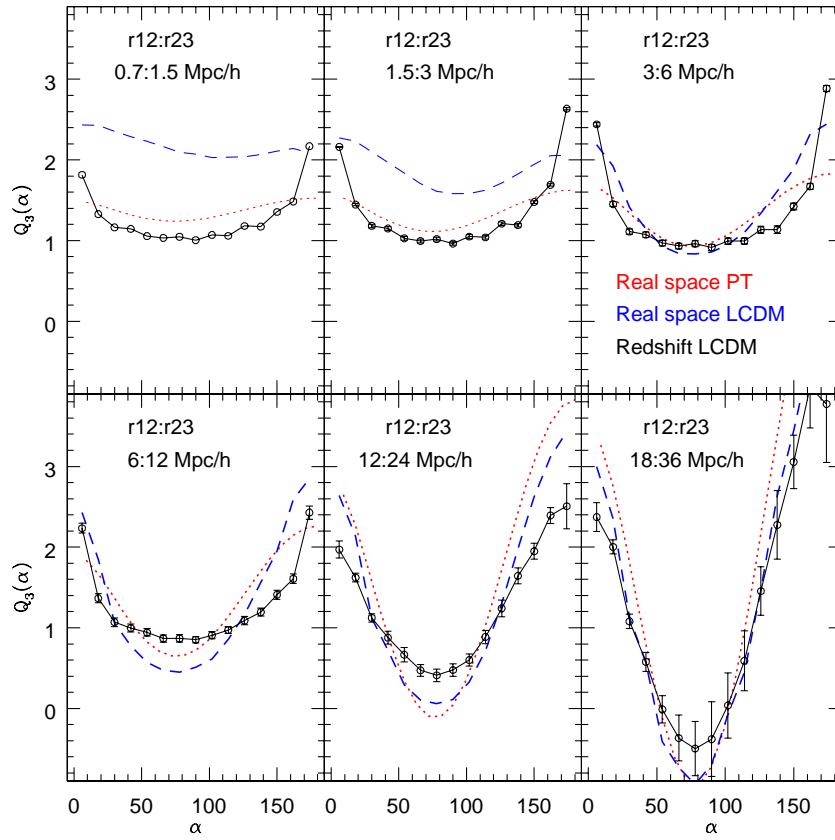


**Figure 2.**  $Q_3(r_{12}, r_{23}, \alpha)$  as a function  $\alpha$ , the angle between  $\vec{r}_{12}$  and  $\vec{r}_{23}$ , in  $\Lambda$ CDM 400 simulations. Real space measurements are shown as dashed lines, while dotted lines show tree-level (real-space) perturbation theory predictions. Symbols with errorbars correspond to redshift space measurements. Each panel shows the results for triangles of different scales.

more realistic situations, including that of a redshift slice (where one of the angular distances, typically declination, is restricted to a few degrees on the sky).

Figure 1 shows a  $1 \text{ Mpc}/h$  slice in the  $\Lambda\text{CDM}240$  case. One can see that:

a) fingers of God are long and sharp needles of about  $1h^{-1}\text{Mpc}$  wide and  $10h^{-1}\text{Mpc}$  long. This should make a very noticeable imprint on  $Q_3$  for elongated triangles (i.e. the "collapsed" configurations in §2.2) across those scales.

b) filamentary structure is apparent on large scales in both cases, although in redshift space it seems to be more washed away. This should show as weaker configuration dependence (or less contrast between collapsed and prependicular triangles) for  $Q_3$  in redshift space than in real space at these large scales.

c) on smaller (non-linear) scales structures are rounder, and seem sharper in real space. Thus, weaker configuration dependence and larger values of  $Q_3$  are expected on small scales in real space.

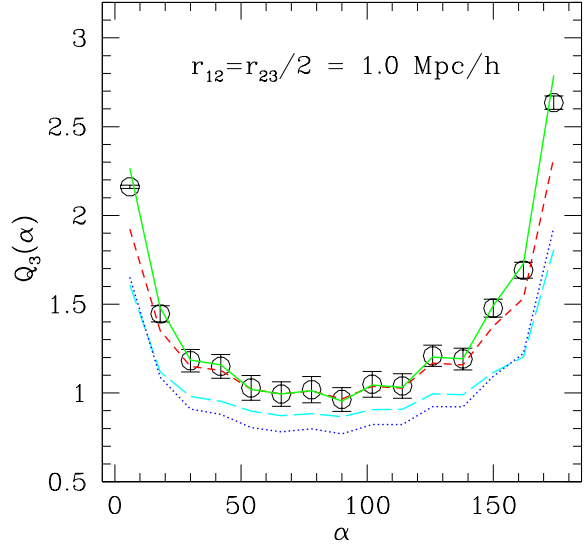
Let's check how these visual impressions are reflected in the actual measurements of  $Q_3$ .

Figure 2 compares the estimations of  $Q_3$  in the  $\Lambda\text{CDM}400$  case for triangles with  $|\vec{r}_{12}| = |\vec{r}_{23}|/2 = 1.5, 3, 6, 9, 12, 18h^{-1}\text{Mpc}$  in real space (dashed lines) and redshift space (symbols with errorbars). The symbols with error-bars show the mean and variance in 5 realizations of the same  $\Lambda\text{CDM}$  simulations, while the dotted lines show the corresponding leading order (tree-level) PT prediction in real space.

On large scales  $Q_3$  in redshift space has only slightly less configuration (or shape) dependence than in real space, as expected from perturbation theory (Hivon et al. 1995) and in agreement with bispectrum results (Scoccimarro et al. 1999), indicating that part of the angular asymmetries are washed out by the peculiar velocities, but this effect is small. Note that on the largest scales  $18 - 36h^{-1}\text{Mpc}$ , the values of  $Q_3$  both in real (or redshift space) seem to approach the PT predictions, within the large errorbars. This provides an important observational test for the current picture of structure formation, independent of cosmological parameters for a fixed power spectrum shape (see Bernardeau et al. 2002).

On scales smaller than  $\leq 10h^{-1}\text{Mpc}$  (where  $\xi > 1$ ), the redshift space results are almost independent of the overall scale of the triangle (despite the large changes in the amplitude of  $\xi$ ), while the real space values increase sharply as a function of scale (at least up to  $\sim 1h^{-1}\text{Mpc}$ ). Note how  $Q_3$  for collapsed configurations  $\alpha \simeq 0, 180 \text{ deg}$  in redshift space rises sharply, while for the perpendicular configurations ( $\alpha \sim 90$ ) the values of  $Q_3$  are quite flat and scale independent. This characteristic anisotropy is what we call the *U-shape*. This U-shape does not appear in real space or in PT theory, as it is basically the results of small-scale redshift distortions, the effect of fingers of God. A similar effect is seen in the small-scale redshift-space bispectrum (see Figs. 3 and 4 in Scoccimarro et al. 1999).

In Fig. 3 we compare the values of  $Q_3$  in redshift space for different models on small scales. The U-shape anisotropy is present in all models regardless of differences in the cosmological parameters. Note also the small errorbars and the good agreement between the two  $\Lambda\text{CDM}$  models with very different resolution (and slightly different  $\sigma_8$  normalization). These results extend to smaller scales: we find very similar



**Figure 3.**  $Q_3(r_{12}, r_{23}, \alpha)$  in redshift space as a function  $\alpha$ , the angle between  $\vec{r}_{12}$  and  $\vec{r}_{23}$ , for simulations in Table 1. Symbols with 3-sigma errorbars (from the scatter in 5 realizations) correspond to  $\Lambda\text{CDM}400$ . Continuous, short dashed, long dashed and dotted lines correspond to  $\text{OCDM}$ ,  $\Lambda\text{CDM}240$ ,  $\text{tCDM}$  and  $\text{SCDM}$  respectively.

results (with no evidence for any change with scale) in the range  $r_{12} = 0.1 - 3 \text{ Mpc}/h$ . All cases in Fig. 3 correspond to  $r_{12} = r_{23}/2 = 1.0 \text{ Mpc}/h$ , except for the  $\Lambda\text{CDM}400$  (symbols with errorbars) which has  $r_{12} = r_{23}/2 = 1.5 \text{ Mpc}/h$ . Figure 4 shows the comparison between  $\Lambda\text{CDM}$  and  $\text{SCDM}$  on different scales. As shown in the figure there is a small global shift between the two models on all scales. On the largest scales, the difference become smaller (in contrast to what happens in real space, see paper I).

The results of Fig. 3 show that the U-shape anisotropy is expected in a wide range of models, and as we will see below (see §5.1) it is also expected in biased galaxy distributions. However, it has not been seen previously in N-body simulations or observations. Early measurements in simulations (Suto & Matsubara 1994, Matsubara & Suto 1994) claimed that the hierarchical ansatz ( $Q_3$  constant independent of configuration and scale) is valid in redshift space at small scales. More recent studies (Jing & Börner 1998) see a very mild effect, but nothing comparable to the amplitude seen in Fig. 3. In observations, similar results are seen in LCRS (Jing & Börner 1998), 2dFGRS (Jing & Börner 2004) and SDSS (Kayo et al. 2004). We believe that these discrepancies with our results are due to these authors' choice of binning, as we discuss now. For example, Matsubara & Suto (1994) bin distances which vary by 30%, Jing & Börner (1998, 2004) have only 5 bins in the  $v$  variable, comparable to Kayo et al (2004), who use 5 bins in  $\alpha$  from 0 to 180 deg.

In order to investigate possible explanations for this situation, we explore the effect of using different pixel resolutions and sparse sampling of triangles. We see in Fig. 5 that this typically results in a biased-low value of  $Q_3$ , significantly so at collapsed configurations. Because there are far fewer triangles in the collapsed configuration, low-resolution trans-

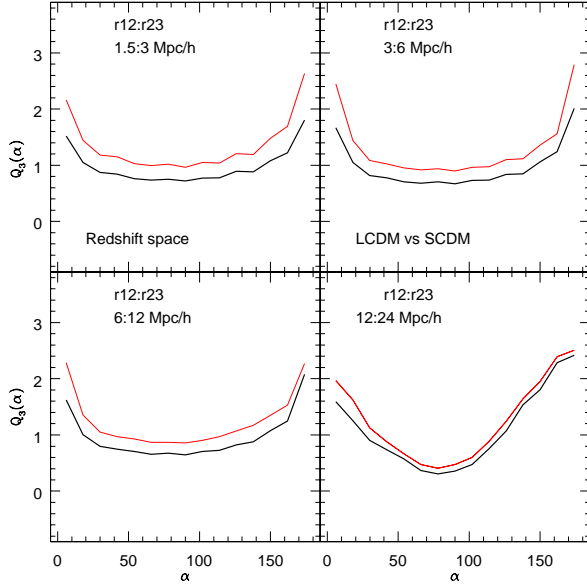


**Figure 4.** Comparison of redshift-space  $Q_3(r_{12}, r_{23}, \alpha)$  for SCDM400 (thick lines) and LCDM400 (thin lines).

lates into a reduced U-shape, effectively mixing a small number of large amplitudes with large numbers of small amplitudes and thus down-weighting the resulting  $Q_3$  at collapsed configurations. A similar effect is obtained if the binning in angle is made too wide; the effect is even more severe in the  $v$ -variable parametrization (see section 2.2) which has been traditionally used at small scales. We believe these reasons may explain why the U-shape anisotropy has not been seen before in the three-point correlation function studies.

## 5 GALAXY BIASING

We now check whether biasing affects significantly the characteristic U-shape dependence we find in redshift space at small scales. We will also study what constraints we can get on biasing parameters from the measurements of  $Q_3$ .

The value of  $Q_3$  depends on galaxy bias, in a form that can be easily calculated on large enough scales, where galaxy fluctuations  $\delta_G$  can be modeled as a local (but non-linear) function of the corresponding matter fluctuations  $\delta$ ; thus expanding this local function for  $\delta \ll 1$  it follows that (Fry & Gaztañaga 1993)

$$\delta_G \simeq F[\delta] \simeq \sum_k \frac{b_k}{k!} \delta^k, \quad (11)$$

where  $k = 0$  comes from the requirement that  $\langle \delta_G \rangle = 0$ . It then follows (see Fry & Gaztañaga 1993, Frieman & Gaztañaga 1994) that:

$$Q_3^G \simeq \frac{1}{b_1} (Q_3 + c_2) \quad (12)$$

where  $c_2 \equiv b_2/b_1$ , and the  $\simeq$  sign indicates that this is the leading order contribution in the expansion given by Eq. (11) above.

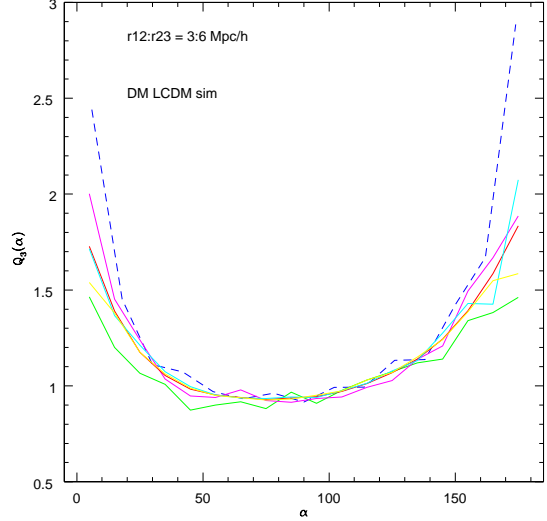


**Figure 5.** Effects of resolution and sparse sampling. The dashed black line shows the result with highest resolution, which gives the higher results for the collapsed configurations ( $\alpha = 0, 180$ ). The lowest line corresponds to the lowest resolution (cubic cells of 1 Mpc/h and sparse sampling of 1 in 10 triangles). Intermediate lines show an increase in resolution by a factor of two (with full sampling).

Thus, in general, the linear bias prescription is not accurate for higher-order moments even when  $\delta \ll 1$ , the reason being that nonlinearities generate non-Gaussianities of the same order as those of gravitational origin. The linear bias term  $b_1$  can produce distortions in the shape of  $Q_3$ , while the non-linear terms  $c_2$  only shifts the curve. Therefore, it is possible to use the shape of  $Q_3^G$  in observations: when compared to the dark matter predictions for  $Q_3$  one can separate  $b_1$  from  $b_2$  in the above relation. This gives an estimate of the linear bias  $b_1$  which is independent of the overall amplitude of clustering (eg.  $\sigma_8$ ). This approach has already been implemented for the skewness  $S_3$  (Gaztañaga 1994, Gaztañaga & Frieman 1994), the bispectrum (Frieman & Gaztañaga 1994, Fry 1994, Feldman et al. 2001, Verde et al. 2002) or the angular 3-point function (Frieman & Gaztañaga 1999).

We now test these ideas with mock galaxy catalogues.

### 5.1 Mock galaxy samples

We use three sets of mock catalogues, which we will call *2dFGRS mocks*, *HV mocks* and *HOD mocks*. Each set has different characteristics which can be used to test the different approximations used.

#### 5.1.1 2dFGRS mocks

The 2dFGRS mocks consist of 22 independent mock 2dFGRS surveys, extracted from the HV simulations (Evrad et al 2002) and described in Norberg et al. (2002). They have the same radial and angular selection function as the final (public) version of the 2dFGRS and have been convolved with the completeness mask of the survey (Cole et al 2005).

We extracted 4 volume limited samples shown in Table 2. These same samples have been used by Baugh et al. (2004) and Croton et al. (2004a,b) to study higher-order moments of counts-in-cells and void probabilities. Unless stated otherwise, we will use as a default the volume limited mock with  $-21 < M_b < -20$ , which yields the best constraints (see Fig.14).

### 5.1.2 HV mocks

These consist of a set of 100 cubic subvolumes of side  $L = 350 \text{ Mpc}/h$ , extracted directly from the HV simulation (see Table 1). There is no galaxy biasing, dilution or realistic mask involved in these mock catalogs. We will use them to estimate close to ideal conditions in a dark matter distribution. The HV mocks each have 2-3 times more effective volume than the 2dFGRS mocks.

### 5.1.3 HOD mocks

We also build galaxy mock catalogs following the results from the measurements of the two-point function in the SDSS (Zehavi et al. 2004). For the thresholds  $M_r < -20$  and  $M_r < -21$ , we use the VLS simulation, and a halo occupation distribution (HOD) prescription for the mean number of galaxies in a halo of mass  $m > m_{\min}$

$$\langle N_{\text{gal}}(m) \rangle = 1 + \left( \frac{m}{m_1} \right)^\alpha \exp[-m_s/(m - m_{\min})], \quad (13)$$

and zero otherwise, where the first contribution is that due to a central galaxy, the rest being satellite galaxies which are taken with a Poisson distributed scatter (Kravtsov et al. 2003). The power-law index  $\alpha$  is fixed to 1. For  $M_r < -19$  and  $M_r < -18$  mock galaxies were kindly provided by A. Berlind, based on the GIF simulation, with the same HOD as in Eq. (13) except for a sharp cutoff at  $m_{\min}$  instead of an exponential cutoff, and the power-law index  $\alpha$  is allowed to vary. The parameters of the HOD's are given in Table 3.

Given a HOD, the expected large-scale bias parameters (in the limit of large scales) are given by,

$$b_i = \frac{1}{n_g} \int dm n(m) \langle N_{\text{gal}}(m) \rangle b_i(m), \quad (14)$$

where  $n(m)$  is the halo mass function (which we take to be that of Sheth and Tormen 2002),  $b_i(m)$  are the corresponding halo bias parameters (Scoccimarro et al. 2001) and the galaxy number density is given by

$$n_g = \int dm n(m) \langle N_{\text{gal}}(m) \rangle. \quad (15)$$

Note how the different absolute magnitude limited samples have different biasing parameters, contrary to what happens in the 2dFGRS mocks, which have a fixed biasing prescription for all magnitude ranges. The main reason for using the HOD mocks is that we know the values of  $b_1, b_2$  that we input in our catalogues, and we can therefore test how well  $b_i$  can be recovered.

Figure 6 shows how well these values of  $b_1$  and  $b_2$  fit the mean biasing scatter relation  $\delta_G = F[\delta]$  in Eq. (11) for cubes of side  $l = 30 \text{ Mpc}/h$  (see also Fig. 1 in Scoccimarro 2000 for more cases). As can be seen in the figure, the agreement

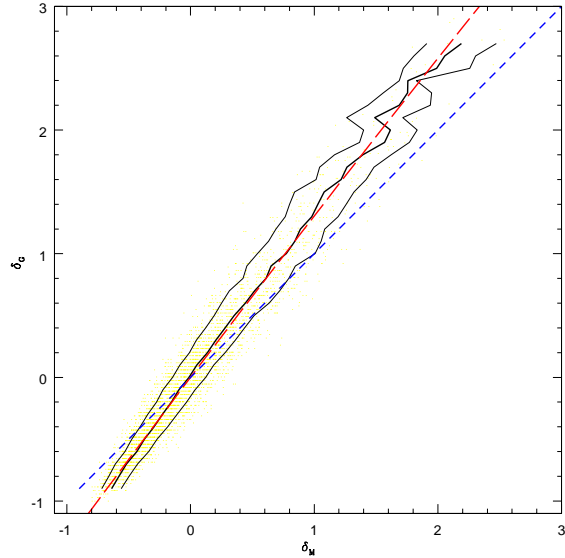


**Figure 6.** Scatter plot showing galaxy density contrast  $\delta_G$  versus dark matter  $\delta_M$  fluctuations in the  $M_r < -20$  HOD sample for cubic cells of side  $l = 30 \text{ Mpc}/h$ . The smooth long-dashed line shows the bias relation with parameters  $b_1$  and  $b_2$  given by the HOD from Eq. (14) with parameters in Table 3. The true mean bias relation is represented by the central thick line and 68% scatter around it (parallel thin lines). The short-dashed line is the unbiased prediction,  $b_1 = 1, b_2 = 0$ .

is quite good. Similar results are found for other smoothing scales:  $l > 15 \text{ Mpc}/h$ . On smaller scales, the scatter plot is dominated by shot-noise (the number of galaxies per pixel becomes too small).

The HOD mocks do not have a realistic survey mask, as in the 2dFGRS mocks, but instead correspond to a simple square box geometry, as in the HV mocks. Given the large size of the VLS simulation (about 3 times in volume the HV mocks) and its simple geometry, a single mock can be used as a prediction for the theoretically expected correlation functions for each set of bias parameters. The 22 2dFGRS and 100 HV mocks will be used to estimate errors and covariance matrices (see §4).

Figure 7 shows a slice corresponding to the HOD mock galaxies with  $M_r < -20$ . Because of the low density we have used a thicker slice here than in the dark matter case of Fig. 1. Note how the fingers of god are not prominent in this case and is hardly possible to detect them visually (compare with Fig. 1). We now study whether we can still detect in  $Q_3$  the signature of fingers of god, the U-shape anisotropy.

## 5.2 Galaxy $Q_3$ : Testing the validity of the bias expansion

Figure 8 illustrates how biasing changes the values of  $Q_3$  from the dark matter simulations (symbols with errors) to the HOD mock galaxies (continuous lines); all quantities here are in redshift space. The errors in the dark matter simulation are obtained from the 100 HV mocks. Similar results are found for other magnitude ranges. Note that the

**Table 2.** Properties of the combined 2dFGRS SGP and NGP volume limited catalogues (VLCs). Columns 1 and 2 give the faint and bright absolute magnitude limits that define the sample. Column 3 gives the median magnitude of the sample, computed using the Schechter function parameters quoted by Norberg et al. (2002). Columns 4, 5 and 6 give the number of galaxies, the mean number density and the mean inter-galaxy separation for each VLC, respectively. Columns 7 and 8 state the redshift boundaries of each sample for the nominal apparent magnitude limits of the survey; columns 9 and 10 give the corresponding comoving distances. Finally, column 11 gives the combined SGP and NGP volume. All distances are comoving and are calculated assuming standard  $\Lambda$ CDM.

Mag. range		Median mag.	$N_G$	$n_g$	$d_{mean}$	$z_{min}$	$z_{max}$	$D_{min}$	$D_{max}$	Volume
$M_{b_J} - 5 \log_{10} h$		$M_{b_J} - 5 \log_{10} h$		$h^3 / \text{Mpc}^3$	$h^{-1} \text{Mpc}$			$h^{-1} \text{Mpc}$	$h^{-1} \text{Mpc}$	$10^6 h^{-3} \text{Mpc}^3$
-18.0	-19.0	-18.44	23290	9.26	0.0048	0.014	0.088	39.0	255.6	2.52
-19.0	-20.0	-19.39	44931	5.64	0.0056	0.021	0.130	61.1	375.6	7.97
-20.0	-21.0	-20.28	33997	1.46	0.0088	0.033	0.188	95.1	537.2	23.3
-21.0	-22.0	-21.16	6895	0.110	0.0209	0.050	0.266	146.4	747.9	62.8

	$M_{min}$	$m_1$	$m_s$	$\alpha$	$n_g$	$b_1$	$c_2$
$M_r < -18$	$1.87 \times 10^{11}$	$3.74 \times 10^{12}$	—	0.92	0.026	0.97	-0.21
$M_r < -19$	$3.87 \times 10^{11}$	$8.8 \times 10^{12}$	—	1.08	0.013	1.07	-0.08
$M_r < -20$	$9.9 \times 10^{11}$	$1.71 \times 10^{13}$	$6.86 \times 10^{12}$	1	0.005	1.13	-0.11
$M_r < -21$	$5.09 \times 10^{12}$	$5.77 \times 10^{13}$	$5.77 \times 10^{13}$	1	0.001	1.32	-0.03

**Table 3.** Parameters of the mean halo occupation distribution used to populate dark matter halos in simulations with mock galaxies, see Eq. (13). All masses are in units of  $M_\odot/h$ . The last three columns correspond to the number density  $n_g$  (in galaxies per  $\text{Mpc}^3 h^{-3}$ ) and bias parameters calculated from Eq. (14), with  $c_2 \equiv b_2/b_1$ .

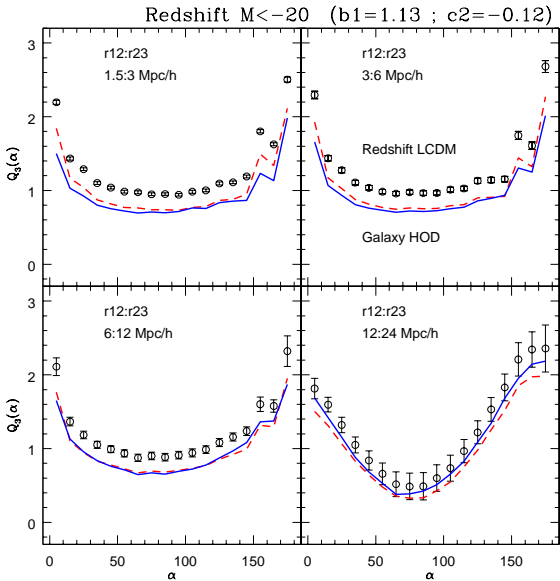


**Figure 8.**  $Q_3$  in redshift space dark matter simulations (points with errorbars, from 100 HV mocks) and respective results for  $M_r < -20$  HOD mocks (continuous line). Dashed lines shows the HOD bias prediction using the values from Table 3 in Eq. (12).

effects caused by biasing at the smallest scales are comparable to the variations among different models shown in Fig. 3. The characteristic U-shape anisotropy due to fingers of god is also present in the galaxy samples on small scales  $r_{12} \leq 6h^{-1} \text{Mpc}$ , even though it is not so obvious to the eye in Fig. 7.

The HOD prediction based on Eqs. (14) and (12) (dashed lines) seems to work very well, even approaching

the non-linear regime the deviations are not too large. Note however that the error bars become very small so these deviations are statistically significant at small scales, as we shall see in more detail below (see eg. bottom panel in Fig. 12). On the other hand, it is encouraging that the validity of the bias expansion seems to be much broader than perhaps naively expected, at least for the galaxy HOD's we have studied here. In this section and below we assume we can trust the local bias expansion, more precisely Eq. (12) for quantities in redshift space, where we always use simulations to make predictions for  $Q_3$  for dark matter in redshift space.

To characterize how well we can recover the actual bias parameters predicted by a given HOD it is necessary as we discuss now to study in detail the covariance between measurements of  $Q_3$  for different triangle shapes and scales.

### 5.3 Q-eigenmodes

As we shall see in the next section, it is reasonable to expect the likelihood function to be Gaussian in terms of  $Q_3$ , at least as a first approximation in the case of large surveys, which means that one can estimate parameters using a  $\chi^2$  approach (likelihood  $\mathcal{L} \propto \exp -\chi^2/2$ ),

$$\chi^2 = \sum_{i=1}^{i=N_b} \sum_{j=1}^{j=N_b} \Delta_i C_{ij}^{-1} \Delta_j \quad (16)$$

with  $C_{ij}$  the normalized (to unit variance) covariance matrix and  $\Delta_i \equiv [Q_3^{obs}(i) - Q_3^{mod}(i)]/\sigma_Q(i)$ , where  $Q_3^{mod}$  corresponds to the model (i.e. Eq. (12) with simulations used to predict the dark matter  $Q_3$ ),  $Q_3^{obs}$  is the measured reduced three-point function of the galaxy population whose bias parameters we want to determine, and  $\sigma_Q$  are the uncertainties in  $Q_3$  which are typically obtained from mock galaxy catalogues (as the diagonal part of the covariance ma-



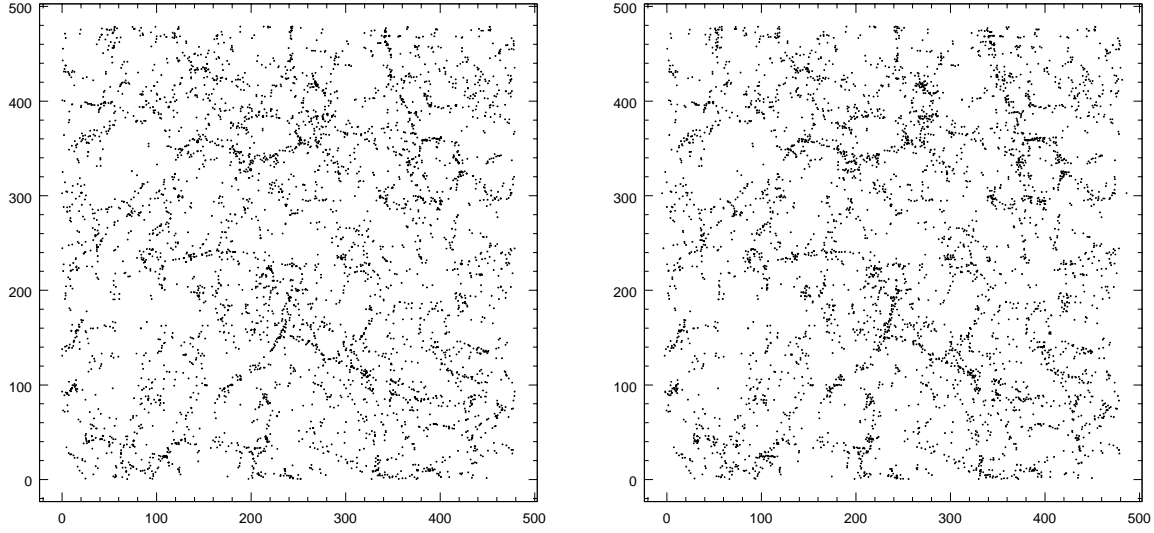


**Figure 7.** Galaxy positions in the real (left) and redshift space (right) in a 5 Mpc/h slice corresponding to HOD mock galaxies with  $M_r < -20$ . The observer is at  $x \rightarrow -\infty$ , just as in Fig. 1.

trix), or estimated directly from the observations eg. using independent sub-samples or jackknife resampling. The label  $i = 1, \dots, N_b$  denotes different triangle shape configurations. In our case, without any loss of generality, we have fixed  $r_{13} = 2r_{12}$  and bins refer only to changes in  $\alpha$  with  $N_b = 18$  (i.e.  $\Delta\alpha = 5$  deg.). In general one could mix many different shape configurations (i.e. different scales) and consider a larger covariance matrix (Scoccimarro 2000).

The normalized covariance matrix is estimated from the mock catalogs as,

$$C_{ij} \equiv \frac{1}{N_m} \sum_{k=1}^{k=N_m} \Delta_i^k \Delta_j^k \quad (17)$$

with  $\Delta_i^k \equiv [Q_3^k(i) - \bar{Q}_3(i)]/\sigma_Q(i)$ , where  $\bar{Q}_3(i)$  is the mean of the  $N_m$  mock independent realizations denoted by the index  $k$ . Figure 9 shows the estimated covariance matrices as a function of the configuration angle  $\alpha$  in triangles of scale  $r_{13} = 2r_{12} = 24$  Mpc/h. As can be seen in this figure, the covariance is quite significant and cannot be neglected. The structure is very similar between the 2dFGRS (top) and HV (bottom) cases.

Before we invert  $C_{ij}$  in Eq. (16), notice that the values of  $C_{ij}$  are estimated in practice to within a limited resolution,

$$\Delta C_{ij} \simeq \sqrt{\frac{2}{N_m}}, \quad (18)$$

therefore if  $N_m$  is small or if there are degeneracies in  $C_{ij}$  the inversion will be affected by numerical instabilities. In order to eliminate this problem, we perform a Singular Value Decomposition (SVD) of the matrix,

$$C_{ij} = (U_{ik})^\dagger D_{kl} V_{lj}, \quad (19)$$

where  $D_{ij} = \lambda_i^2 \delta_{ij}$  is a diagonal matrix with the singular values on the diagonal, and  $U$  and  $V$  are orthogonal matrices that span the range and nullspace of  $C_{ij}$  (see Eisenstein & Zaldarriaga 2001, for an application to the power spec-

trum estimation). By doing the SVD decomposition, we can choose the number of modes we wish to include in our  $\chi^2$  by effectively setting the corresponding inverses of the small singular values to zero. In practice, we work only with the subspace of “dominant modes” which satisfy:

$$\lambda_i^2 > \sqrt{2/N_m} \quad (20)$$

which is the resolution to which we can estimate the covariance matrix elements. In other words, when doing the inverse of  $C$  in Eq. (16), one inverts Eq. (19) with a restriction on  $D_{kl}$  based on the criterion given by Eq. (20).

Within the Gaussian assumption one needs to go no further than what we have discussed to obtain constraints on bias parameters. However, Gaussianity must be checked for each particular survey and scale under study. As shown for the bispectrum (Scoccimarro 2000), the non-Gaussian case can be simplified by rotating into the basis where the  $Q_3$ 's become diagonal, and their non-Gaussian distributions can be obtained from mock catalogs and multiplied together effectively assuming that they are independent to construct the likelihood function for the bias parameters.

In other words, one can represent each of the mock or data  $Q_3$  vectors (the vector index  $i = 1, N_b = 18$  runs over different values of  $\alpha$  in this case) in a new basis of Q-eigenvectors where the covariance matrix becomes diagonal (since  $U$  is the rotation matrix for nonzero modes ),

$$\hat{Q}_3(i) = \sum_j U_{ji} \frac{Q_3(j)}{\sigma_Q(j)}, \quad (21)$$

The data expressed in the new basis, the  $Q$ -eigenmodes  $\hat{Q}_3$ , is a vector which in general has a lower dimensionality than  $N_b$  due to the criterion given by Eq. (20). Contrary to  $Q_3$ , the Q-eigenmodes are effectively statistically independent (this becomes rigorous in the Gaussian case), in the sense that their covariance matrix is diagonal. The eigenvalues  $\lambda_i^2$  are the diagonal elements of their covariance matrix, i.e.

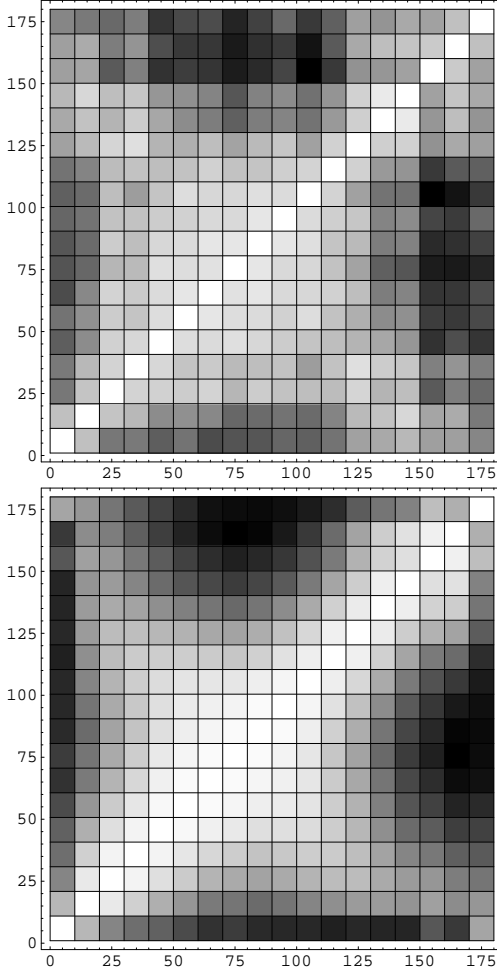


**Figure 9.** Normalized covariance matrix  $C_{ij}$  as a function of the configuration angle  $\alpha$  (in degrees) from  $Q_3(\alpha)$  for fixed side triangles with  $r_{13} = 2r_{12} = 24$  Mpc/h. White and black colours corresponds to +1 and  $-1$  covariance, respectively. Middle grey corresponds to zero values. The top panel shows the covariance matrix from 22 2dFGRS mocks, while the bottom panel is obtained from the 100 HV mocks.

the variance of a given Q-eigenmode. One can construct a “signal to noise” (S/N) for each eigenmode labeled by  $i$ ,

$$\left(\frac{S}{N}\right)_i = \left| \frac{\hat{Q}_3(i)}{\lambda_i} \right| = \left| \frac{1}{\lambda_i} \sum_{j=1}^{N_b} U_{ji} \frac{Q_3(j)}{\sigma_Q(j)} \right|. \quad (22)$$

The total S/N can be obtained by adding the individual modes in quadrature. When we use only the dominant Q-eigenmodes, the total S/N estimate corresponds to a lower bound, which is not optimal, but avoids potential errors of a singular inversion. Figure 10 shows the three most important (in terms of signal to noise) Q-eigenvectors for the case of the HV mocks at scales  $r_{13} = 2r_{12} = 24$  Mpc/h. As can be seen in the figure the Q-eigenvectors correspond to interesting linear combination of different triangles: the first mode (solid) is basically the average  $Q_3$  (slightly down-weighted for collapsed configurations, which have larger errors), the second eigenmode (short-dashed) measures the difference between collapsed and perpendicular configurations, this is sensitive to the dependence of  $Q_3$  on triangle shape,

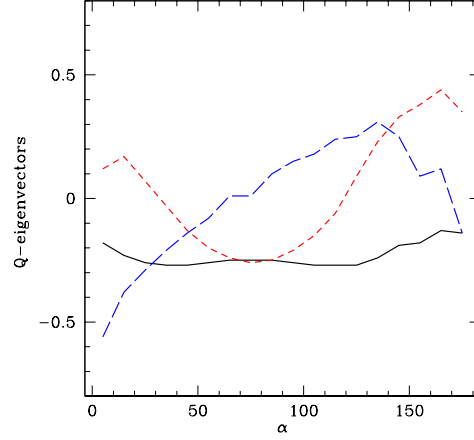


**Figure 10.** The three dominant, in terms of signal to noise [see Eq. (22)] Q-eigenvectors for triangles with  $r_{13} = 2r_{12} = 24$  Mpc/h from 100 HV mock catalogs. The signal-to-noise values are 9.1 (solid), 8.4 (short-dashed), and 8.0 (long-dashed).

the third eigenvector (long-dashed) gives the difference between the configuration dependence at small and large  $\alpha$  (down-weighted on the largest scales because of the large errors), this is sensitive to the scale dependence of  $Q_3$ . The behavior of the eigenvectors shown in Fig. 10 is completely analogous to what was found in the bispectrum case (see Fig. 16 in Scoccimarro 2000). The condition in Eq. (20) is satisfied by 6 Q-eigenmodes (individual signal-to-noise values are  $S/N = 9.1, 8.4, 8.0, 6.7, 4.9$  and 1.1) in this particular case with a total signal-to-noise of  $S/N = 17.0$ . Later, in section 5.5 and Figs. 12-14, we will illustrate the use of the Q-eigenmodes to recover the bias parameters.

#### 5.4 Gaussianity of the Likelihood Function

A central assumption we made above is that the Q-eigenmodes are Gaussian distributed. This can *and should always* be checked against numerical realizations of the particular survey geometry and scales being studied, otherwise the outcome of the likelihood analysis could be significantly biased, even if the covariance between different triangles is taken into account. Here we explore the validity of the Gaussian likelihood approximation for the three-point function, extending similar studies done for the bispectrum (Scoccimarro 2000) and higher-order moments (Szapudi et al. 2000).

As the survey volume increases, for a triangle of given scale and shape, the Gaussian approximation should become better as more such triangles contribute to its  $Q_3$  and although one is adding correlated quantities, one naively expects to reach the central limit theorem if the correlations are small. However, it is not obvious this is enough because at the same time the error bars for the bias parameters shrink, and thus a small systematic bias (if comparable to the small error bars) can still affect the determination of parameters. A simple rule of thumb is to compute the skewness of the distribution of  $Q_3$  and check whether this is much smaller than the shift in  $Q_3$  that results from displacing  $b_1, b_2$  by the error bars, if so the systematic error that

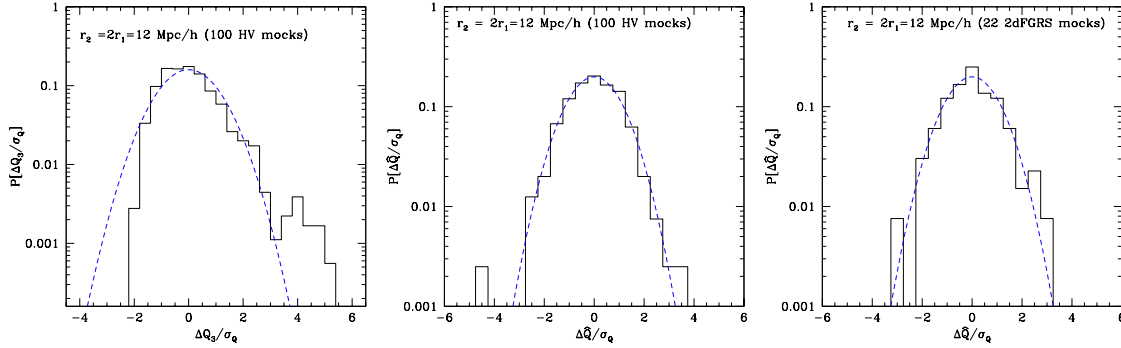


**Figure 11.** Histograms comparing the measured distribution of 3-point amplitudes  $Q_3$  (normalized to have unit variance) to the expected Gaussian distribution. The left panel corresponds to the 100 HV mocks, which results in a slightly skewed non-Gaussian distribution. The middle panel shows the distribution for the 5 dominant Q-eigenmodes  $\hat{Q}$  using the same data, which is much more Gaussian. The right panel shows the first 5 dominant Q-eigenmodes  $\hat{Q}$  in the 22 2dFGRS mocks. All cases correspond to triangles with fixed sides  $r_{12} = 2r_{13} = 12$  Mpc/h and different values of  $\alpha$ .

results from assuming Gaussianity can perhaps be safely ignored (see discussion in Hui & Gaztañaga 1999, Scoccimarro 2000 and Szapudi et al. 2000 for more details).

Here we compare the histograms of values of  $Q_3$  in the galaxy mocks to a normalized Gaussian distribution: for each triangular shape,  $\alpha$ ,  $r_{12}$  and  $r_{13}$ , we estimate the mean value of  $Q_3$ ,  $\bar{Q}_3$ , and its variance  $\sigma_Q^2$  in the mock catalogs. We then build a histogram of  $(Q_3 - \bar{Q}_3)/\sigma_Q$  values for different realizations and also different configuration angles  $\alpha$ , but with fixed  $r_{12}$  and  $r_{13}$  sides. Although in general the distribution is not far from a Gaussian, it sometimes shows significant deviations.

The left panel in Fig. 11 shows the worst situation we have encountered in our study. The distribution is somewhat skewed, although this is not a large effect (notice the logarithmic scale). This is much more reassuring than the analogous result for IRAS surveys (see e.g. Fig. 15 in Scoccimarro 2000) where the distribution becomes strongly non-Gaussian for smaller galaxy samples. In our case, the 2dFGRS or HV mocks are large enough to avoid these severe biases and the Gaussian likelihood seems a good approximation, but the distribution still has some small degree of skewness. In the left panel in Fig. 11 the dimensionless skewness of the distribution is +1.1, which translates in a bias of about 10% in the estimated  $Q_3$ .

The relevant distribution in our method is not so much the distribution of  $Q_3$ , but the distribution of the Q-eigenmodes. These are shown in the middle (HV mocks) and right (2dFGRS mocks) panels of Fig. 11 (notice the change in vertical scale from the left panel). The distribution seems better approximated by a Gaussian, which is expected since these are the highest signal to noise modes and should approach Gaussianity fastest. The results correspond to triangles with fixed sides  $r_{12} = 2r_{13} = 12$  Mpc/h, but similar results are found for other scales. The dimensionless skewness in both cases is of order 0.1, much smaller than in the direct distribution of  $Q_3$ . This translates into 1% bias in  $Q_3$ , which is smaller than the sampling variance from the single HOD mock.

We conclude that a Gaussian likelihood provides a good approximation for our particular situation, specially when we express our results in terms of Q-eigenmodes. We will

therefore use the Gaussian  $\chi^2$  test in Eq. (16), restricted to the subspace of the dominant Q-eigenmodes from the SVD criterion, Eq. (20)

## 5.5 Recovering Bias Parameters

Figure 12 shows how well we can recover the values of  $b_1$  and  $c_2$  using the measurements of  $Q_3$  for  $r_{13} = 2r_{12} = 6, 12$  and  $24h^{-1}$  Mpc assuming that the clustering pattern follows that of the  $M_r < -20$  HOD mock galaxies. We use two different sets of mock catalogs (HV and 2dFGRS) to estimate the error bars and Q-eigenmodes to assess the sensitivity of each survey geometry. The mean values for the dark matter and galaxy  $Q_3$  are from the same simulation (VLS). From inside out, the values of the contours denote  $\Delta\chi^2 \equiv \chi^2 - \chi^2_{min} = 2.4, 6.2, 11.8$  away from the minimum  $\chi^2$  value in Eq. (16), corresponding to 1, 2 and 3 $\sigma$  confidence intervals for a  $\Delta\chi^2$  distribution with two free parameters. Each panel also displays the total S/N, according to Eq. [22], added in quadrature for the dominant Q-eigenmodes used in each case.

As can be seen in Fig. 12, there is a main direction that is best determined corresponding to the first eigenmode, this is basically the direction perpendicular to the line  $(Q_{avg} + c_2)/b_1 = \text{const.}$  where  $Q_{avg}$  is the average value of  $Q_3$ . As small scales are approached,  $Q_3$  develops the characteristic U-shape anisotropy and if the errors do not decrease fast enough (top panel) a near degeneracy develops in the  $b_1 - c_2$  plane. The reason is that  $b_1$  scales the shape dependence of  $Q_3(\alpha)$ , while  $c_2$  only shifts the curve up or down. In the limit where the "U" is made of vertical and horizontal lines alone, scaling ( $b_1$ ) and shifting ( $c_2$ ) produce equivalent (degenerate) effects. For large scales, the contours become wide because of the lack of enough independent triangles. As a result of these two limits, the best configurations for constraining the  $b_1 - c_2$  parameter space in 2dFGRS are those at intermediate scales ( $r_{13} = 2r_{12} = 12h^{-1}$  Mpc).

The crossed circle in Fig. 12 corresponds to the  $b_1, c_2$  expected for the input galaxy mock catalogues using the HOD predictions in Eq. (14). These predictions are also shown as dashed lines in Fig. 8 and provide a very good description

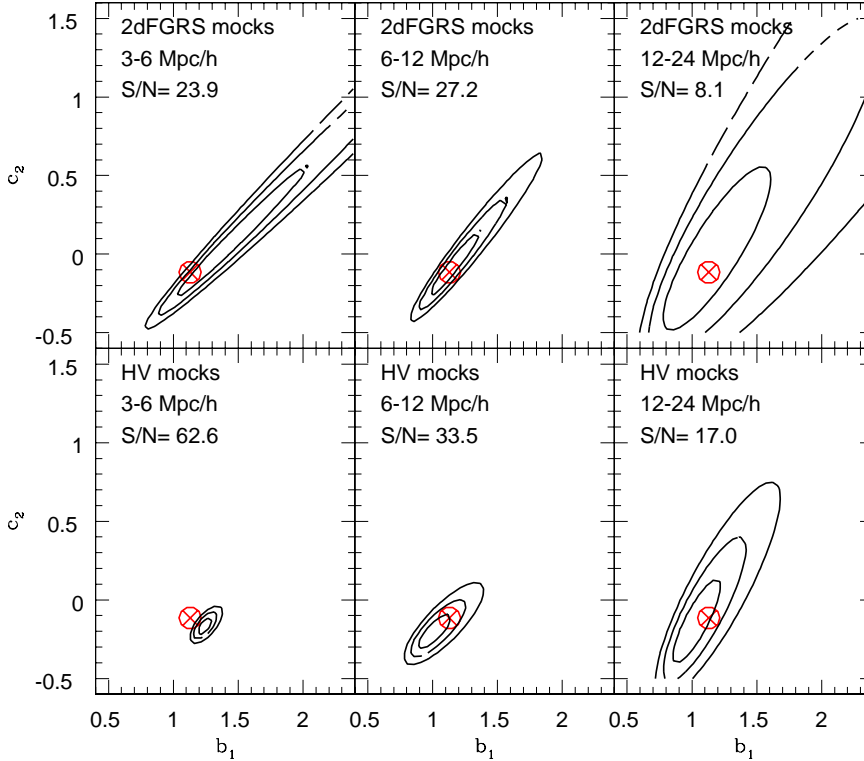


**Figure 12.** Constraints on  $b_1$  and  $c_2$  for triangles of different scales, as labeled in each panel. In all cases we compare measurements of  $Q_3$  in dark matter simulations to galaxy HOD mock catalogs. The top panels use errors (and Q-eigenmodes) from 2dFGRS mocks, while the bottom panels use HV mocks (smaller contours because HV have 2-3 times the effective volume of 2dFGRS mocks).

of the mean bias relation, at least on large scales. Note that there are no free parameters here, we are not fitting for  $b_1$  and  $c_2$ , but rather checking we recover the values used for  $b_1$  and  $c_2$  to create the mock catalogs using parameters in Table 3. Also recall that we are using a single HOD mock (from VLS simulations) to test the predictions, which means that there is some variance in the estimation and we should not expect the crossed circle on top of the best fit value.

On smaller scales, our treatment of biasing breaks down because one can no longer use the expansion in Eq. (11) nor the simple HOD predictions based on Eq. (14). This failure can be seen in the bottom left panel of Fig. 12, where one finds significant ( $> 3\sigma$ ) deviations from the predicted values.

Figure 13 illustrates the importance of using the dominant Q-eigenmodes, specially when we only have a small number of mock catalogs or samples to estimate the covariance matrix. As illustrated by the top right panel, if a noisy covariance matrix is inverted directly one recovers the incorrect values with unrealistically small error bars due to numerical instabilities. When we restrict the number of Q-eigenmodes the errors become larger (compare top and bottom left panels), but the estimation is not biased by the number of mocks used (compare two bottom panels). Note how the S/N is wrongly estimated in the top right panel and corresponds to a lower estimate when we use only the dominant Q-eigenmodes.

Finally, Fig. 14 shows the constraints for different volume limited samples for the 2dFGRS mocks. The case

$-21 < M_b < -20$  provides the best compromise between sample volume and number density. The brighter sample has more volume, but is dominated by shot-noise. The fainter samples with higher density do not cover a large enough volume. These results are qualitatively similar to Fig. 9 in Sefusatti & Scoccimarro (2004).

## 6 CONCLUSIONS

We have studied the three-point function amplitude  $Q_3$  in dark matter and mock galaxies with particular emphasis on the effects of redshift-space distortions and galaxy biasing.

Whereas the dependence of  $Q_3$  on triangle shape is partially erased in redshift space on large scales  $r_{12} > 10h^{-1}\text{Mpc}$ , at smaller scales  $Q_3$  develops a characteristic U-shape anisotropy due to the effects of velocity dispersion. This is expected based on visual inspection of the distribution in redshift space (the finger of God effects). But nevertheless, it has not been detected before in simulations nor observations. We studied why this is so and concluded that low resolution in the configuration angle  $\alpha$  can suppress this sharp feature due to mixing of collapsed configurations (which are few) with the more numerous (with much less amplitude) configurations away from  $\alpha = 0, 180$  deg. This problem can be exacerbated by using the  $v$  parameter as a probe of angle (instead of  $\alpha$ ), which has been a common choice in small-scale studies. Moreover, errors are largest for

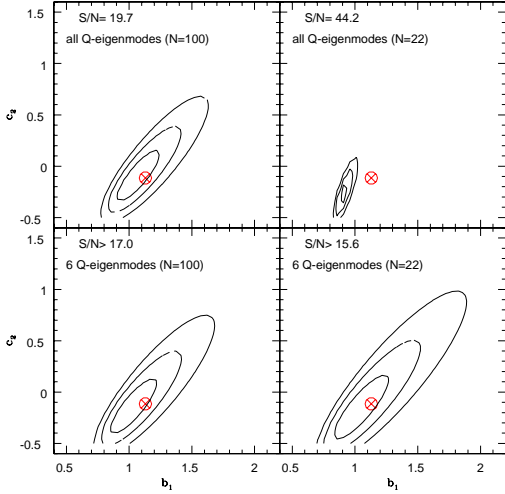


**Figure 13.** Constraints on  $b_1$  and  $c_2$  using the data in Fig. 8 ( $M_r < -20$ ) at  $r_{13} = 2r_{12} = 24h^{-1}\text{Mpc}$ . The input values (in Table 3) are denoted with a crossed circle. The top panels use all the Q-eigenmodes (equivalent to a direct inversion of the covariance matrix), while the bottom panels use only the dominant Q-eigenmodes (Eq.[20]). Left panels use 100 HV mocks while right panels use only the first 22 HV mocks. Using the direct covariance inversion with too few mock catalogs (top right panel) typically gives systematically biased results and unrealistically small error-bars and large S/N.

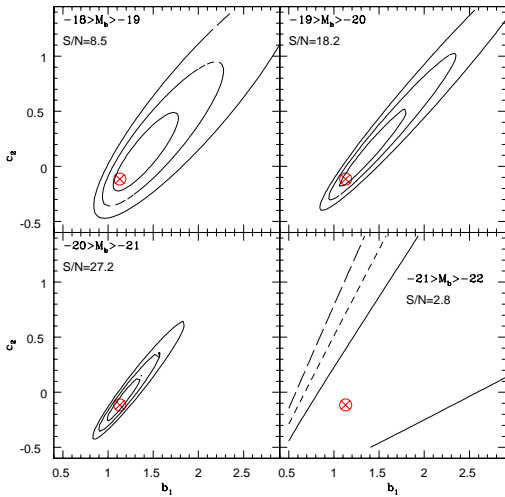


**Figure 14.** Constraints on  $b_1$  and  $c_2$  from realistic 2dFGRS mocks (using the dominant Q-eigenmodes) of different absolute magnitudes (the volume-limited samples in Table 2). Here we only use triangles with  $r_{13} = 2r_{12} = 12h^{-1}\text{Mpc}$ .

the collapsed configurations, which both makes it more difficult to detect and is subject to larger estimation biases.

Our detection of the U-shape anisotropy is completely analogous to the results from the small-scale bispectrum, which shows a very similar effect (Scoccimarro et al. 1999), and we see it in every cosmological model and including galaxy bias (see Figs. 3, 8). We therefore conclude that the redshift-space three-point function *does not* follow the hier-

archical ansatz at small scales (less than 6 Mpc/h), much less so than in real-space, contrary to statements in the literature. On the other hand, the *scale* dependence of  $Q_3$  is weakly suppressed in redshift-space when compared to real-space, thus if the U-shape anisotropy of  $Q_3$  is missed due to poor resolution, a hierarchical three-point function becomes a good model.

We presented a detailed method for obtaining constraints on galaxy bias parameters from measurements of  $Q_3$  in current galaxy redshift surveys, based on the Q-eigenmode analysis developed for the bispectrum (Scoccimarro 2000). We showed that the covariance matrix of  $Q_3$  has non negligible extra diagonal components and presented an SVD inversion method that can be stable even if too few mock catalogs are used for the computation of the covariance matrix, with the only drawback in this case being an overestimate of the error bars. We studied the Gaussianity of the likelihood function and showed that for surveys such as 2dFGRS Gaussianity is a good approximation for the distribution of the Q-eigenmodes, although some small skewness is present.

We discussed the sensitivity of  $Q_3$  to bias parameters as a function of the scale included in the analysis, and presented results for how well we can expect to recover the linear and quadratic bias parameters in the case of 2dFGRS. We showed that our method recovers the bias parameters introduced into mock galaxies by an HOD prescription and is also able to handle potential systematics in case a smaller number than ideal of mock catalogs is used to estimate the covariance matrix.

## ACKNOWLEDGMENTS

We thank Andreas Berlind for making available to us the SDSS mock catalogs corresponding to  $M < -18$  and  $M < -19$  and Naoki Yoshida for help with the VLS simulations. We also thank Carlton Baugh, Darren Croton and Peder Norberg for making the 2dFGRS and HV mocks available and for comments to the manuscript. We acknowledge support from the Spanish Ministerio de Ciencia i Tecnologia, project AYA2002-00850 with EC-FEDER funding and grants NSF PHY-0101738 and NASA NAG5-12100. R. S. thanks the Kavli Institute for Cosmological Physics at the University of Chicago for hospitality during a sabbatical visit. The GIF, VIRGO, VLS and HV simulations in this paper were carried out by the Virgo Supercomputing Consortium using computer s based at the Computing Centre of the Max-Planck Society in Garching and at the Edinburgh parallel Computing Centre. The data are publicly available at <http://www.mpa-garching.mpg.de/NumCos>

## REFERENCES

- Barriga, J. & Gaztañaga, E. , 2002, MNRAS, 333, 443
- Baugh, C.M. et al., MNRAS, 351, L44, 2004
- Baugh C. M., Gaztanaga E., 1996, MNRAS, 280, L37
- Baumgart, D.J. & Fry, J.N., ApJ., 375, 25, 1991
- Berlind, A.A. et al., ApJ., 593, 1, 2003
- Bernardeau, F., Colombi, S., Gaztañaga, E., Scoccimarro R., Physics Reports, 367, 1, 2002

- Bouchet, F.R., Strauss, M.A., Davis, M., Fisher, K.B., Yahil, A., Huchra, J.P., ApJ, 417, 36, 1993
- Colless, M. et al, MNRAS, 328, 1039, 2001
- Colombi, S., Szapudi, I., Szalay, A.S., MNRAS, 296, 253, 1998
- Cooray, A., Sheth, R., Physics Reports, 372, 1, 2002
- Croton, D.J. et al., MNRAS, 352, 828, 2004a
- Croton, D.J. et al., MNRAS, 352, 1232, 2004b
- Eisenstein D. J., Zaldarriaga M., 2001, ApJ, 546, 2
- Evrard A. E., et al., 2002, ApJ, 573, 7
- Feldman, H.A., Frieman, J.A., Fry, J.N., Scoccimarro, R., Phys. Rev. Lett., 86, 1434, 2001
- Frieman, J.A., Gaztañaga, E., ApJ., 425, 392, 1994
- Frieman J.A., Gaztañaga E., ApJ, 521, L83-L86, 1999 .
- Fry, J.N., Peebles, P.J.E., ApJ., 221, 19, 1978.
- Fry, J. N., Phys. Rev. Letters, 73, 2, 1994.
- Fry, J.N., Gaztañaga, E., ApJ., 425, 1-13, 1994.
- Gaztañaga, E., ApJ., 398, L17-L20, 1992.
- Gaztañaga, E., MNRAS, 268, 913, 1994.
- Gaztañaga, E., Frieman, J.A., ApJ., 437, L13, 1994
- Groth, E.J., Peebles, P.J.E., ApJ., 217, 385, 1977.
- Hivon, E., Bouchet, F.R., Colombi, S. and Juszkiewicz, R., A&A, 298, 643, 1995
- Hui, L., Gaztañaga, E., ApJ., 519, 622, 1999
- Jing, Y.P., Börner, G., ApJ., 503, 37, 1998.
- Jing, Y.P., Börner, G., ApJ., 607, 140, 2004
- Kaiser, N., MNRAS., 227, 1, 1987.
- Kayo, I. et al., Pub. Astron. Soc. J., 56, 413, 2004
- Jackson, J.C., MNRAS., 156, 1, 1972.
- Ma C.P., Fry, J.N., ApJ., 543, 503, 2000.
- Matsubara, T., Suto, Y., ApJ., 420, 504, 1994.
- Matarrese, S., Verde, L., Heavens, A.F., MNRAS, 290, 651, 1997.
- Norberg, P. et al., MNRAS, 336, 907, 2002
- Peacock J.A., Smith, R.E., MNRAS., 318, 1144, 2000.
- Peebles, P.J.E., Groth, E.J., ApJ., 196, 1-11, 1975.
- Peebles, P.J.E., 'The Large Scale Structure of the Universe', Princeton, Princeton University Press, 1980.
- Sargent, W.L.W., and Turner, E.L. ApJ(Lett.), 212, L3, 1977
- Scoccimarro R., Couchman, H.M.P. and Frieman, J.A., ApJ, 517, 531, 1999.
- Scoccimarro R., ApJ, 544, 597, 2000.
- Scoccimarro, R., Sheth, R.K., Hui, L. and Jain, B. ApJ., 546, 20, 2001
- Scoccimarro, R., Sefusatti, E., Zaldarriaga, M., Phys.Rev.D69, 103513, 2004
- Sefusatti, E., Scoccimarro, R., astro-ph/0412626, 2004
- Seljak, U., MNRAS., 318, 203, 2000.
- Sheth, R.K., Tormen, G., MNRAS, 329, 61, 2002
- Suto, Y., Matsubara, T., ApJ., 420, 497, 1994.
- Szapudi, I., Colombi, S. Bernardeau, F., MNRAS, 310, 428, 1999
- Szapudi, I., Colombi, S. Jenkins, A., Colberg, J., MNRAS, 313, 725, 2000
- York, D.G. et al, AJ, 120, 1579, 2000
- Verde, L. et al., MNRAS, 335, 432, 2002
- Wang, Y, Yang, X., Mo, H.J., van den Bosch, F.C., Chu Y., 2004 arXiv:astro-ph/0404143.
- Zehavi, I. et al., arXiv:astro-ph/0408569.